

## Cold electron sources using laser-cooled atoms

This content has been downloaded from IOPscience. Please scroll down to see the full text.

View [the table of contents for this issue](#), or go to the [journal homepage](#) for more

Download details:

IP Address: 128.250.144.144

This content was downloaded on 29/07/2016 at 12:02

Please note that [terms and conditions apply](#).

# Cold electron sources using laser-cooled atoms

Andrew J McCulloch<sup>1</sup>, Ben M Sparkes<sup>1</sup> and Robert E Scholten

School of Physics, The University of Melbourne, 3010, Australia

E-mail: [scholten@unimelb.edu.au](mailto:scholten@unimelb.edu.au)

Received 7 March 2016, revised 4 June 2016

Accepted for publication 22 June 2016

Published 29 July 2016



CrossMark

## Abstract

Since the first observation of electron diffraction in 1927, electrons have been used to probe the structure of matter. High-brightness sources of thermal electrons have recently emerged that are capable of simultaneously providing high spatial resolving power along with ultrafast temporal resolution, however they are yet to demonstrate the holy grail of single-shot diffraction of non-crystalline objects. The development of the cold atom electron source, based around the ionisation of laser cooled atoms, has the potential to contribute to this goal. Electron generation from laser cooled atoms is in its infancy, but in just ten years has moved from a proposal to a source capable of performing single-shot diffraction imaging of crystalline structures. The high brightness, high transverse coherence length, and small energy spread of cold electron sources are also potentially advantageous for applications ranging from seeding of x-ray free-electron lasers and synchrotrons to coherent diffractive imaging and microscopy. In this review we discuss the context which motivates the development of these sources, the operating principles of the source, and recent experimental results. The achievements demonstrated thus far combined with theoretical proposals to alleviate current bottlenecks in development promise a bright future for these sources.

Keywords: cold electrons, laser cooling, ultrafast diffraction, coherent diffractive imaging

(Some figures may appear in colour only in the online journal)

## 1. Introduction

### 1.1. Towards the molecular movie

Our understanding of materials and processes has evolved with our ability to probe and alter systems at ever-decreasing spatial and temporal scales. The ultimate limit to this would be to image individual atoms, and to be able to monitor their interactions with the environment on atomically relevant time-scales. Laser systems have progressed to single femtosecond pulse lengths, allowing for the study of simple atomic systems with unprecedented timing resolution [1–4], including direct observation of molecular vibrations [5].

The interaction between laser radiation and samples only occurs when the characteristic length scales, the

wavelength and atomic spacing(s), are similar. To achieve atomic resolution, therefore, either electrons or hard x-rays must be used for illumination, and it is here that the great challenge lies: to produce sub-picosecond radiation pulses with sub-nanometre imaging resolution and sufficient signal-to-noise to produce individual frames for a ‘molecular movie’. If we had such a source it would allow us to perform single-shot diffraction of sensitive biological samples before damage can occur, critical for determining the structure and evolution of biologically relevant targets such as membrane proteins [6, 7].

The brightness required for single-shot diffraction of individual molecules may never be achieved, but increasing coherence and brightness will allow structure determination using smaller or imperfect crystals [8] and faster structure determination than using cryo electron microscopy [9–11]. Brighter electron sources are needed as injectors for next-generation x-ray free electron lasers (XFELs) and

<sup>1</sup> These authors contributed equally to this work.

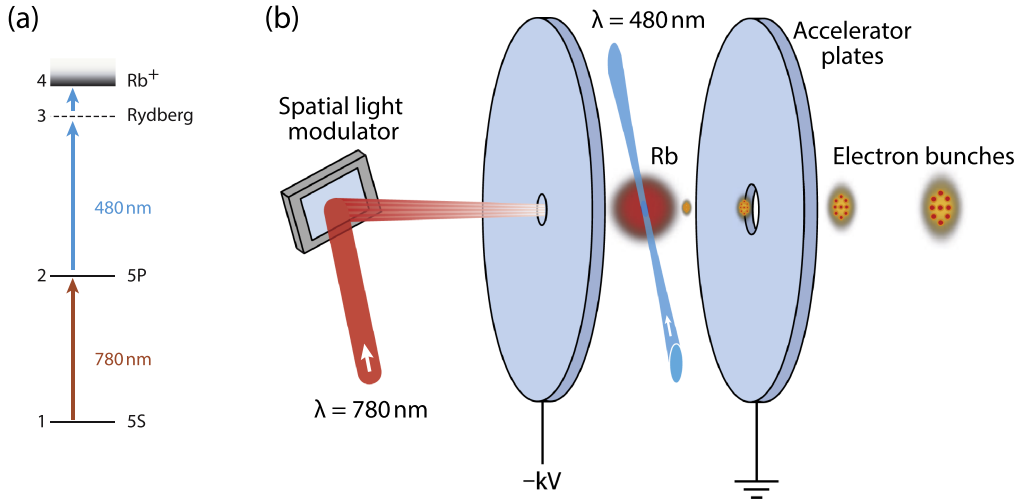


**Figure 1.** (a) Photo-excitation/ionisation level structure for  $^{85}\text{Rb}$ . (b) Cold atom electron source based on a cloud of laser-cooled rubidium atoms (Rb) located between two accelerator plates (trapping lasers not shown). Adapted with permission from [15].

synchrotrons and for coherent diffractive imaging (CDI) of non-crystalline targets [12–14]. Cold atom electron sources (CAESs) are a promising alternative for the next generation of such applications.

### 1.2. Electrons produced from cold atoms

The desirable qualities of the CAES (figure 1) stem from the minimal thermal energy imparted to the electrons upon formation. Conventional sources of electrons have either relied upon thermionic emission (tungsten or lanthanum hexaboride) or field emission (cold cathode or Schottky) for electron production, both of which produce electron beams with an appreciable energy spread. In contrast, electrons from a CAES are produced by carefully photoionising a sample of cold neutral atoms, either directly or by field-assisted ionisation via excitation to a high-lying Rydberg state, resulting in electrons with near negligible thermal energy. The photoionisation process can be exploited to further improve the source properties, for example to control in real time the density distribution of the electron beam through modulation of the laser intensity distribution, which in turn can be used to alleviate otherwise irreversible Coulomb expansion of the beam. The low temperature of the electron bunches makes them highly focusable with a large transverse coherence length, necessary for diffraction imaging. Another significant point of difference between the CAES and conventional sources is that both electrons *and* ions are produced, and many of the same advantages are of more direct importance for focused ion beam devices as recently reviewed in [16].

We begin by describing the important performance metrics of an electron beam 2.1, followed by a discussion of progress in thermal source development to date in section 2.2. A detailed discussion of the CAES is then presented in section 3 before we explore some of the areas of research currently of most interest to the community, namely overcoming beam degradation due to heating effects (3.2) and inter-beam Coulomb repulsion (3.3), and recent proof-of-principle electron diffraction experiments in section 4.

## 2. Beam theory and sources

### 2.1. Beam quality metrics

The quality of an electron beam is assessed in different ways depending on the application. Beam quality metrics facilitate the comparison of electron sources, but can be illuminating in their own right, helping to understand why a particular source is appropriate for a given application.

**2.1.1. Brightness:** The brightness of an electron beam is the current density per unit solid angle in the axial direction. It is the primary requirement for high resolution imaging in both time and space simultaneously. The transverse brightness  $\mathcal{B}_\perp$  of a beam is given by

$$\mathcal{B}_\perp = \frac{\mathbf{J}}{d\Omega} = \frac{dI}{dSd\Omega}, \quad (1)$$

where  $\mathbf{J}$  is the current density,  $\Omega$  is the solid angle subtended by the beam,  $I$  is the beam current and  $S$  is the cross section of area occupied by the beam. It is common to refer to the average brightness  $\bar{\mathcal{B}}_\perp$ , which is integrated over  $dS$  and  $d\Omega$ ; and the normalised brightness  $\bar{\mathcal{B}}_{n\perp} = \bar{\mathcal{B}}_\perp / (\beta\gamma)^2$  with  $\beta = v_z/c$  and  $\gamma = 1/\sqrt{1-\beta^2}$ , where  $v_z$  is the mean longitudinal electron velocity. The normalised brightness is invariant and is used for the comparison of electron beams of different energy.

To gain an appreciation for the brightness, consider a beam of current  $I$  with a mean divergence angle of  $\Delta\theta$ . If a beam of radius  $R$  is focused through a lens of focal length  $f$ , it can be shown that the power density at the focus is [17]

$$|\mathbf{J}| \simeq \frac{\pi}{4} \left( \frac{f}{2R} \right)^{-2} \frac{I}{(\pi R \Delta\theta)^2} \sim \frac{\bar{\mathcal{B}}_\perp}{[f^*]^2}, \quad (2)$$

where  $f^*$  denotes the  $f$ -number of the lens. Thus the power density at the focus is proportional to the beam brightness and, therefore, brightness will be the constraining factor on imaging speed and resolution.

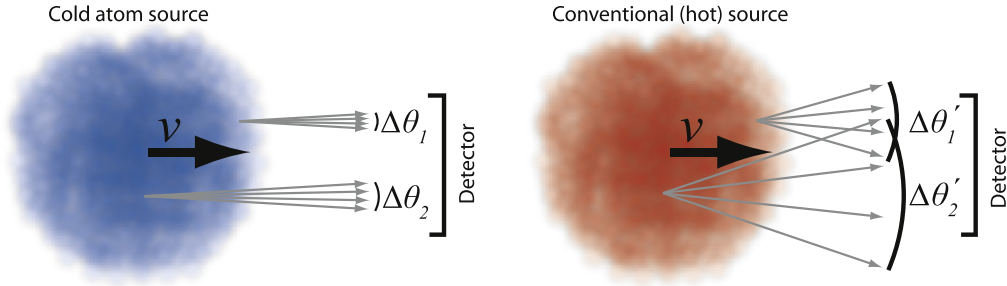


**Figure 2.** Illustration of the difference in angular distribution from a cold versus a conventional (hot) source of electrons: the cold electrons have a much smaller angular spread  $\Delta\theta$ . This small spread results in a much larger transverse coherence length (equation (7)). Adapted with permission from [19].

For a thermal electron source, the solid angle of a paraxial beam is

$$\int_0^{2\pi} \int_0^\theta d\Omega \approx \frac{\pi}{v_z} \sqrt{\frac{k_B T}{m_e}}, \quad (3)$$

where  $m_e$  is the electron mass and hence

$$\mathcal{B}_{n\perp} = \frac{\mathbf{J} mc^2}{4\pi k_B T}. \quad (4)$$

This is the *maximum* achievable brightness for electrons at a temperature  $T$ . The solid angle will usually be greater than for a paraxial beam and hence the brightness lower. The benefit of using cold electrons is obvious from the inverse relationship between temperature and brightness. In this form it is clear that the brightness depends on the current density and a high brightness can be realised with low current.

Another variant of brightness is the reduced brightness  $\mathcal{B}_r$ , used mainly for non-relativistic electron microscopy sources, where the minimum spot size is more important than the total current. This can be expressed in terms of the transverse brightness [18]

$$\mathcal{B}_r = \frac{2e\mathcal{B}_\perp}{mc^2}. \quad (5)$$

**2.1.2. Coherence:** Diffraction imaging requires phase coherence across the transverse area of the object to be imaged, for example a unit cell of a crystalline material. The coherence length  $\mathcal{L}_c$  characterises the length scale of the spatial correlations within the electron beam at a given propagation distance (figure 2), placing restrictions on the size of the object to be illuminated. The transverse coherence length can be written as

$$\mathcal{L}_c = \frac{\lambda}{2\pi\sigma_\theta}, \quad (6)$$

where  $\lambda$  is the de Broglie wavelength and  $\sigma_\theta$  is the root mean square (rms) angular spread of the source. Assuming that the electrons are in thermal equilibrium, equation (6) can be recast as

$$\mathcal{L}_c = \frac{\hbar}{\sqrt{m_e k_B T}}. \quad (7)$$

Propagation over large distances and isolating a small fraction of the beam, e.g. using an aperture, will increase the transverse coherence length as a consequence of the Van Cittert-Zernike theorem [20] but will be accompanied by a commensurate loss of flux. Ideally, the transverse coherence at the source should be large enough such that no flux need be lost to achieve a required transverse coherence length at the sample. For single-shot diffraction of microcrystals the transverse coherence length at the sample must be on the order of a few lattice spacings and, for maximum signal-to-noise, the total beam size should match the sample size. This can be quantified in terms of the relative transverse coherence length at a focus [21]

$$C_\perp = \frac{\mathcal{L}_c}{\sigma_0}, \quad (8)$$

where  $\sigma_0$  is the initial rms size of the electron bunch. It should be noted that in principle, aberrations present in the lens system do not degrade the coherence properties [22].

Above we assume that the coherence length does not vary as a function of spatial frequency. A more detailed model has been developed [23], where it was assumed the electron source was thermally equilibrated and comprised of mutually incoherent point radiators each of which radiates into a small angular distribution. It was shown that the source has a Gaussian coherence function with a coherence length of  $\hbar/\sqrt{m_e k_B T}$ , consistent with equation (7).

**2.1.3. Emittance:** Emittance is a measure of the *effective* phase space volume occupied by a particle beam, which fundamentally limits its brightness. Formally, the transverse rms normalised emittance  $\epsilon_x$  is defined by

$$\epsilon_x \equiv \frac{1}{m_e c} \sqrt{\langle x^2 \rangle \langle p_x^2 \rangle - \langle x p_x \rangle^2}, \quad (9)$$

where  $m_e$  is the electron mass,  $x$  is the transverse position with  $x = 0$  the average position of the bunch and  $p_x$  is the transverse electron momentum. The  $\langle \dots \rangle$  indicates the ensemble average taken over all particles in the beam.

Experimentally, one usually does not directly measure the momentum spread, but rather an angular spread. Defining  $x'$  as the angle a particle makes with the beam axis of symmetry,  $x' = v_x/v_z$ , provided the beam is paraxial  $v_x \ll v_z$ ,

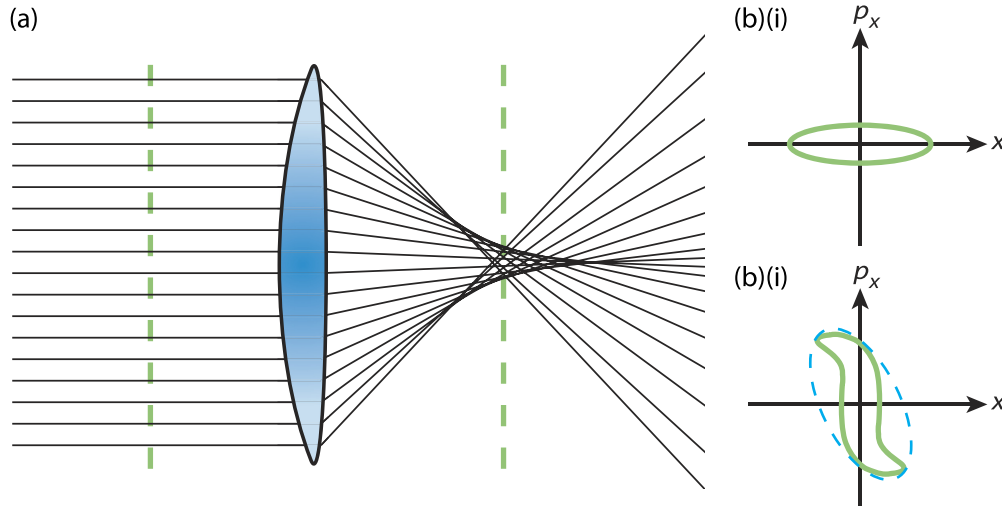


**Figure 3.** (a) A beam is incident upon an imperfect lens, resulting in a paraxial focus. (b) Phase-space distributions of the incident beam (i) and at the focus (ii). The area of the ellipse in (i) determines the transverse beam emittance before the lens. The distorted shape of (ii), however, leads to an increase in the effective phase space volume (dashed ellipse) and, therefore, to the emittance.

the emittance can be expressed as

$$\epsilon_x = \gamma\beta\sqrt{\langle x^2 \rangle \langle x'^2 \rangle - \langle xx' \rangle^2} \equiv \gamma\beta\bar{\epsilon}_x. \quad (10)$$

Recasting the emittance as equation (10) is convenient, as  $\bar{\epsilon}_x$  is a measure of the trace-space volume of the beam, and can be measured experimentally.

If the electron source is in thermal equilibrium, the radial emittance becomes

$$\bar{\epsilon}_{r,n} = \sigma_r \sqrt{\frac{k_B T}{m_e c^2}} \quad (11)$$

for an rms bunch radius  $\sigma_r$ . Emittance is related to focusability, with a smaller emittance leading to a smaller  $\sigma_r$  at a bunch focus. From equation (11) we can see that having a small initial source size or a low temperature will both lead to a smaller initial bunch emittance.

Emittance increases with increases in the phase space volume of the beam due to irreversible processes. In the context of particle optics, a reversible process is one that preserves not only phase space volume, but also the continuity of the distribution. Irreversible processes lead to a distortion of the phase-space ellipse, as shown in figure 3. We can define an *effective* volume as the smallest elliptical phase space distribution that can encompass the actual distribution.

Identifying the angular spread as  $\sigma_\theta = \bar{v}_{x,\text{th}}/v_0 = \bar{x}/\bar{\epsilon}_x$  from equation (11), the coherence length (equation (6)) can be re-expressed as

$$\mathcal{L}_c = \frac{\lambda}{2\pi\sigma_\theta} = \frac{\hbar}{m_e c} \frac{\sigma_r}{\bar{\epsilon}_r}. \quad (12)$$

Similarly, using equation (11), the brightness can be related to the emittance via equation (4) to give

$$\mathcal{B}_{n\perp} = \frac{\mathbf{J}}{4\pi} \frac{mc^2}{k_B T} = \frac{I}{4\pi^2 \bar{\epsilon}_r^2}. \quad (13)$$

Knowledge of the beam emittance therefore allows for determination of the coherence length and brightness, as well as being a useful quantity for comparison between sources.

## 2.2. Current generation sources

Electron and x-ray sources are both promising, and complementary, candidates for imaging of single molecules. While the theory of diffraction is qualitatively identical for all waves, the interaction between different sources of illumination and matter varies dramatically. X-rays are weakly interacting and scatter primarily from the inner shell electrons of atoms, whereas electrons interact very strongly, scattering from both the electrons and atomic nuclei, necessitating very thin samples. In this section we discuss established electron sources and provide an overview of x-ray sources.

**2.2.1. X-ray sources:** XFELs are very bright sources of x-ray pulses, based on self-amplified spontaneous emission, where the shot-noise from an ultra-short, high brightness relativistic electron bunch [24] is used to seed the creation of x-rays in a single-pass configuration from a linear accelerator [25–27]. Current XFEL sources can have pulse durations as short as 10 fs [28] with brightnesses on the order of  $10^{33}$  photons  $\text{s}^{-1} \text{mm}^{-2} \text{mrad}^{-2}$  [29]. Importantly for diffractive imaging, XFELs possess a high degree of transverse coherence [30].

Single-shot coherent diffraction imaging with an XFEL was first performed by Chapman *et al*, where they imaged a nanostructured non-periodic silhouette, which was subsequently destroyed by the x-ray bunch [31]. The same group then demonstrated single-shot diffraction of nanocrystals of Photosystem I with dimensions of 200 nm–2  $\mu\text{m}$  using femtosecond pulses [32]. Other results achieved with XFELs include single-shot imaging of single minivirus particles [7], lysozyme microcrystals [33], sub-micron living *Microbacterium lacticum* cells [34], and Photosystem II [35].

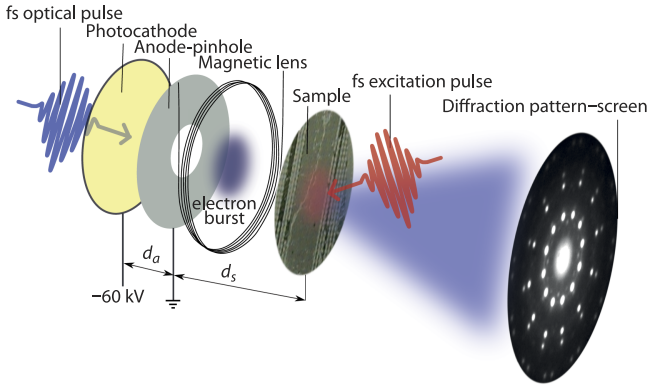


**Figure 4.** Components of a photoelectron gun used to produce sub-picosecond pulses of electrons. Here a femtosecond optical pulse (blue) is incident on a gold photocathode at a potential of  $-60$  kV. The electrons are accelerated to the anode, which is grounded, and apertured to increase the coherence length at the expense of bunch charge. They are then focused by a magnetic lens onto the sample and the diffraction pattern is imaged on a screen. The excitation pulse (red) is present for pump-probe experiments. For the experiment shown here  $d_a = 6$  mm and  $d_s = 2.4$  mm. The compact nature of the source is designed to minimise degrading space-charge effects. Reproduced from [37].

**2.2.2. Electron sources:** The use of electrons for imaging single molecules and nanocrystals is appealing due to the stronger scattering displayed by electrons, reducing the brightness required to achieve single-shot ultrafast electron diffraction (UED). Therefore, what would require billions of dollars and a particle accelerator for x-ray diffraction could conceivably be replicated with a table-top electron source, making the ability to perform single-shot imaging of non-crystalline samples widely available and affordable.

The use of electrons, however, provides other challenges. In single-shot UED, each bunch must contain sufficient charge to produce a measurable diffraction pattern, of order  $10^6$  electrons/pulse [36], coupled with pulse durations well below 1 picosecond. Also, to achieve low emittance and therefore a highly focusable electron bunch from a thermal

source (i.e.,  $T = 10^3$  to  $10^4$  K) requires a very small source area (equation (11)). These factors combined lead to an explosion in electron bunch size due to repulsive Coulomb interactions within the bunch. This space-charge driven expansion degrades the quality of the beam, reducing the transverse focusability and temporal resolution, as discussed in greater detail in section 3.3.

In 2003 Siwick *et al* developed a compact photoelectron gun source that was the first to demonstrate sub-ps electron bunches. With a source similar to that shown in figure 4, they were able to observe the melting of aluminium, with 150 shots per diffraction pattern [38]. Since then, few- [39, 40] and single-shot [36, 41–43] UED of crystalline samples has been demonstrated using photoelectron guns, as discussed in more detail in section 4. For photocathode sources  $\mathcal{B}_r \approx 10^7$  A m<sup>-2</sup> sr<sup>-1</sup> V<sup>-1</sup>.

While these sources can produce the necessary charge with the required temporal resolution they have poor transverse coherence, insufficient for imaging of single molecules or nanocrystals. Continuous sources of electrons, for example field emission sources, can be used to produce beams with sufficient coherence length, however imaging is necessarily slow. The electrons produced from photoelectron guns have temperatures greater than 1000 K and a source size on the order of  $100 \mu\text{m}$ , giving a relative transverse coherence length  $C_\perp$  on the order of  $10^{-6}$  (see table 1), too small for imaging of protein microcrystals, which requires  $C_\perp$  between  $10^{-5}$  and  $10^{-3}$  [12, 44, 45].

Low emittance sources can be created by ensuring the emission area is small, but the associated strong Coulomb interactions within the small emission region limit the maximum electron current that can be extracted without impacting the beam brightness. For instance, carbon nanotubes produce a current of  $1 \mu\text{A}$  from an area of a few  $\text{nm}^2$  to achieve a reduced brightness of  $\mathcal{B}_r = 10^{12}$  A m<sup>-2</sup> sr<sup>-1</sup> V<sup>-1</sup> [46, 47]. The same principle is true of other high-brightness electron sources such as cold field emission guns (CFEG- $\mathcal{B}_r = 10^9$  A m<sup>-2</sup> sr<sup>-1</sup> V<sup>-1</sup>), Schottky emitters

**Table 1.** Table of values from ultrafast electron diffraction experiments, comparing thermal photocathode sources (PC) to cold atom-based sources (CAES).  $C_\perp$  is the relative transverse coherence length (equation (8)). Bracketed terms indicate the bunch charge post-aperture.

Reference	Source type	Bunch length (rms)	Bunch charge (Electron number)	Shots	Bunch energy	Source size (rms)	$C_\perp$
[38]	PC	600 fs <sup>a</sup>	$6 \times 10^3$	150	30–40 keV	200 $\mu\text{m}$ <sup>a</sup>	$2 \times 10^{-6}$
[39]	PC	200 fs <sup>a</sup>	$6 \times 10^3$	10	55 keV		
[40]	PC	350 fs <sup>a</sup>	$1 \times 10^4$	4–12	55 keV		
[41]	PC	10 ps <sup>a</sup>	$4 \times 10^5$ ( $6 \times 10^4$ )	1	340 keV	1.7 $\mu\text{m}$	$3 \times 10^{-4}$
[42]	PC	2.3 ps	$8.75 \times 10^7$ ( $2 \times 10^6$ )	1	2.76 MeV	60 $\mu\text{m}$	$8 \times 10^{-6}$
[43]	PC	250 fs <sup>a</sup>	$6.25 \times 10^7$ ( $1 \times 10^7$ )	1	3.5 MeV	500 $\mu\text{m}$	$1 \times 10^{-6}$
[36]	PC	<100 fs	$1.25 \times 10^6$	1	95 keV	63 $\mu\text{m}$ <sup>b</sup>	$8 \times 10^{-6}$
[71]	CAES	2.5 ps	100s	1,000	10–13 keV	32–54 $\mu\text{m}$	$2 \times 10^{-4}$
[74]	CAES	5 ns	$5 \times 10^5$	1	8 keV	425 $\mu\text{m}$	$2 \times 10^{-5}$

<sup>a</sup> Assumes quoted bunch size is rms.

<sup>b</sup> Rms radius calculated assuming semicircular transverse distribution of radius  $100 \mu\text{m}$ .

( $\mathcal{B}_r = 10^8 \text{ A m}^{-2} \text{ sr}^{-1} \text{ V}^{-1}$ ) [48], LaB<sub>6</sub> nanowires ( $\mathcal{B}_r = 10^{11} \text{ A m}^{-2} \text{ sr}^{-1} \text{ V}^{-1}$ ) [49], and single atomic site emitters ( $\mathcal{B}_r \leq 10^{11} \text{ A m}^{-2} \text{ sr}^{-1} \text{ V}^{-1}$ ) [50, 51]. These sources are particularly useful for scanning electron microscopy where high brightness and very low emittance allow tight focusing to extremely small (sub-Å) probe size. An ideal source for microscopy would have very low emittance, an energy spread below 0.1 eV to reduce chromatic aberration, and maintain a current above 1 nA [52].

Low emittance electrons can also be produced with cryogenically cooled emitters. Recently, an alkali antimonide Cs<sub>3</sub>Sb photocathode was cooled to 90 K, yielding a reduction in emittance of nearly 25% compared to a room-temperature source [53]. The mean transverse kinetic energy for the emitted electrons was measured to be approximately 20 meV, approximately half that of the room temperature cathode. This is still much larger than the values achieved using cold atom sources, typically 1 meV or below; however the current delivered by an alkali antimonide photocathode is much greater than that of a cold atom source.

### 3. Laser cooled sources

The advent of laser cooling and trapping [54–57] heralded a new era for the preparation of atoms in a particular internal and external state. Reaching temperatures of microKelvin and below allowed ensembles of Doppler-free atoms to be addressed and manipulated. Numerous reviews on laser cooling and applications have been published (e.g. [58]). The key points relevant for this work are that laser cooling provides a pathway to both cool and trap neutral atoms and that these processes have been demonstrated for at least 27 different atomic species.

The benefit of using charged particles produced from cold atoms was demonstrated with magneto-optically trapped-target recoil ion momentum spectroscopy [59], an extension of cold target recoil ion momentum spectroscopy [60] that provides high resolution momentum images of atomic and molecular ionisation of atoms and molecules. A near-negligible velocity distribution of the atoms ensures that any momentum spread measured amongst the ions after ionisation is due only to the ionisation process. In 2005 it was suggested that electron and ion beams produced from cold atoms would similarly benefit from the low velocity spread of the source [61], enabling the production of high quality charged particle beams. This was motivated by the dramatic improvements to bunch brightness, coherence length and emittance that would occur with a reduction in temperature by approximately three orders of magnitude.

The first electron source based on laser cooled atoms was realised in 2007 using rubidium [65] and the first ion source was created in 2008 [66] using chromium. Lithium ion [67] and additional rubidium ion [15, 68] sources followed. These sources were based around a three dimensional magneto-optical trap (MOT) with an accelerating structure incorporated into the trap.

Claessens *et al* used a MOT with four conductive rods surrounding the trapped atoms allowing for an accelerating field to be applied across the trapping region [65]. The same group, motivated by the possibility of generating short duration electron pulses, moved to a design optimised for rapidly switching the accelerating field [69]. The system was still centred around a MOT, but the electric field required for acceleration and extraction of the electrons was provided by a coaxial structure which surrounded the trapped atoms. This set-up is shown in figure 5(a) and has allowed for the demonstration of the suitability of CAES(s) for single-shot electron diffraction [70], the production of ultrafast electron bunches [45] and UED [71], in addition to investigating ionisation dynamics [72].

McCulloch *et al* used another design for a CAES whereby the accelerator forms part of the optical system used to create a MOT at its centre [62], as shown in figure 5(b). The accelerator consists of a transparent indium tin oxide (ITO) electrode and a gold electrode which is used to reflect some of the cooling laser beams required to the MOT, a design which was previously used for the creation of a cold ion beam [66]. The apparatus of McCulloch *et al* demonstrated electron bunch shaping [62], ultrafast bunch generation [73], detailed space charge dynamics [15] and most recently, single-shot electron diffraction [74].

Another apparatus, shown in figure 5(c), is centred around an ac-MOT [75] and has been proposed with the goal of using the electron bunches as injection pulses for high energy accelerators [63]. More recently, there has been a push to also develop sources based on laser cooled atomic beams [64, 76–78] (figure 5(d)), which are highly appealing for the creation of high brightness ion beams, primarily due to an increased atomic flux compared to a MOT source.

Multiple different measurements have been made of the transverse temperature [45, 62, 70], coherence length [19] and emittance [73] of the various CAES set-ups described. These are all consistent, with a minimum temperature of 10 K for the electrons measured, a corresponding coherence length of approximately 10 nm at the source, and a source emittance of down to 1 nm rad for a bunch rms width of 30 μm [71]. Combining a source size of tens of micrometres, with a coherence length of 10 nm gives a relative transverse coherence length of  $C_{\perp} = 10^{-3}$ , the right order of magnitude for imaging of protein microcrystals [45].

The largest bunch charge reported to date is 80 fC ( $5 \times 10^5$  electrons) [74], sufficient for single-shot ultrafast diffraction from gold. With an effective source width of 1.4 mm FWHM, this corresponds to a peak transverse brightness of  $\mathcal{B}_{\perp} = 3 \times 10^8 \text{ A m}^{-2} \text{ sr}^{-1}$ . Figure 6 shows a comparison of the expected performance of a CAES with actual calculations from the cold atom diffraction imaging experiments [71, 74], as well as other, thermal, sources in terms of transverse brightness and longitudinal energy spread. It can be seen that the normalised brightness of the Eindhoven CAES [70] is higher than RF photoelectron guns and XFELs, while the Melbourne CAES [73] is approximately equal. For UED applications [80, 81], where a high bunch charge is required, a trade-off must be made between transverse

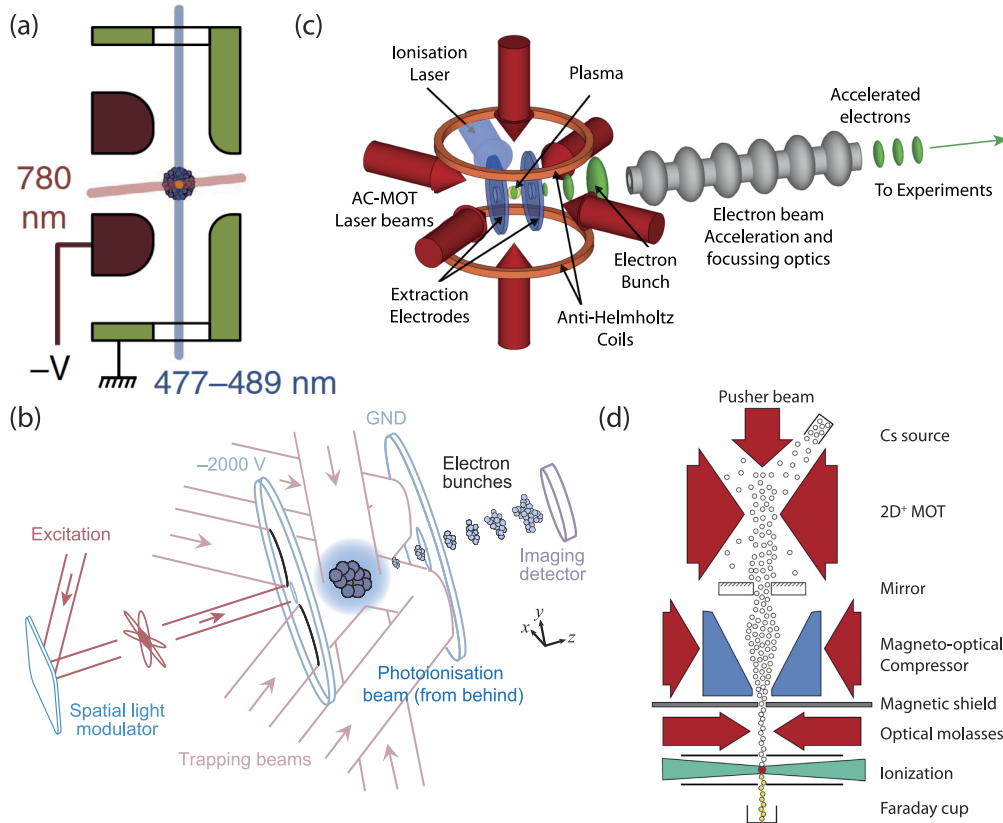


**Figure 5.** Different implementations of the cold atom electron source: (a) design optimised for rapid switching of the accelerator field; (b) using accelerators as part of the optical system (one transparent, one reflective) with the potential for transverse bunch shaping; (c) based upon an ac-MOT; and (d) a continuous atom-beam source. Adapted with permission from [45, 62, 63] and [64] (Copyright 2013, American Institute of Physics.) respectively.

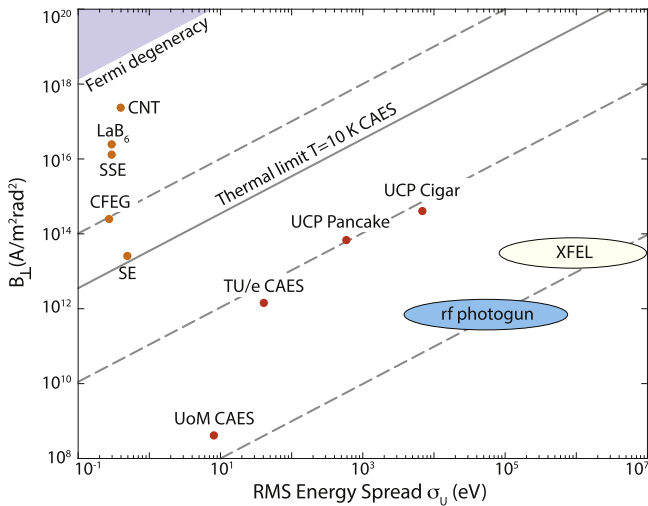


**Figure 6.** Comparison of thermal sources to CAES sources showing transverse brightness  $B_{\perp}$  versus longitudinal rms energy spread  $\sigma_U$ . UCP pancake corresponds to simulated ellipsoidal bunches with uniform electron density initially much shorter in  $z$  than in the transverse direction, and cigar refers to a simulated ellipsoidal bunch with the  $z$  length much longer than the transverse length (see section 3.3). Dashed lines indicate constant normalised brightness. CNT: carbon nanotube; LaB<sub>6</sub>: LaB<sub>6</sub> nanowire; SSE: single site emitters; CFEG: cold field emission guns; SE: Schottky emitters; UoM CAES: University of Melbourne CAES used for single-shot diffraction imaging [74]; TU/e CAES: Eindhoven University of Technology CAES used for ultrafast diffraction imaging [71]. Adapted with permission from [79].

coherence and longitudinal energy spread, limited by the atomic density and ionisation efficiency. The relatively low brightness of the Melbourne CAES is due to a combination of the relatively high initial emittance (because a large excitation area was used to generate a large bunch charge,  $5 \times 10^5$  electrons) and the relatively slow ionisation pulse (5 ns compared to 100 fs for the Eindhoven CAES). An ultrafast high brightness CAES has also been suggested for use as an injector for a compact XFEL [82]. In both CAES implementations, the longitudinal energy width is determined by the longitudinal ( $z$ ) length of the ionisation region.

### 3.1. Ionisation mechanisms

A key element of a CAES is the method of ionisation. Ideally this will be done in a way that minimises excess energy transfer to the electrons and occurs on a femtosecond time-scale. Photoionisation of cold atom clouds and the subsequent evolution of the ensemble have been studied in detail in the context of ultracold plasmas, in an effort to create a strongly coupled plasma. The concept of producing such plasmas via photoionisation of neutral atoms was first investigated in the early 1970s [83], but not realised until many years later. In 1999, the creation of the first UCP via the near-threshold ionisation of metastable xenon was reported [84]. The field rapidly evolved, combining the extensive research that has

been conducted in the field of plasma physics with the much newer field of cold atom physics.

To date, most CAESs has been produced via the photoionisation of magneto-optically trapped atoms. Typically an atomic ensemble in the ground state is excited to an intermediate state and a pulsed laser (5 ns) is used to couple the intermediate state to a high-lying Rydberg state or the ionisation continuum. Photoexcitation usually occurs in an electric field with direct ionisation to a Stark-shifted continuum threshold. The electric field also accelerates the electrons in the primary beam propagation direction. The ionisation scheme allows for the excess thermal energy of the electrons to be carefully tuned by controlling the ionisation laser wavelengths and, in addition, the laser beam intensity profiles for both excitation and ionisation can be manipulated allowing for tailoring of the electron density distribution to shape the electron bunches (section 3.3). The level of control demonstrated by these experiments enables the production of electrons many orders of magnitude colder than conventional sources, and thus for the production of high brightness electron pulses.

The excess energy of the electrons  $\Delta E$  will depend on the wavelength of the ionisation laser  $\lambda$  via [85]

$$\Delta E = hc \left[ \frac{1}{\lambda} - \left( \frac{1}{\lambda_0} - 4\text{Ry} \sqrt{\frac{F}{F_0}} \right) \right], \quad (14)$$

where  $\lambda_0$  is the wavelength of the field-free ionisation energy, Ry is the Rydberg constant,  $F$  is the magnitude of the external electric field and  $F_0$  is the atomic unit for the electric field. The longitudinal energy spread  $\sigma_U$  for this ionisation process will depend on the longitudinal width of the ionisation region,  $\sigma_z$  and the electric field strength

$$\sigma_U = e\sigma_z F. \quad (15)$$

The dynamics of the ionisation of hydrogenic systems in external electric fields has been studied in detail in the context of Rydberg ionisation [86], photoemission and photo-detachment [87–89]; it is worth noting that the underlying mathematics are equivalent to a satellite under the influence of constant acceleration in the presence of an attractive gravitational body [90]. A series of publications on photoionisation microscopy have detailed the ionisation dynamics of an electron wavepacket in a combined Coulomb and strong external field both classically [91] and quantum mechanically [92], showing excellent agreement with experiment [93, 94].

A similar treatment has been developed in the context of a CAES [72] to show that the combined Coulomb and external electric field leads to a *reduction* in the transverse momentum spread of the electrons for below-threshold ionisation. When photoionisation occurs below the field-free threshold, the presence of the saddle point in the potential restricts which transverse velocity components will result in the electron escaping the potential of the parent ion (figure 7). In this way, the effective source temperature can be controlled. This is an important result on the way to realising UED with cold atom sources as, if one were to ionise the

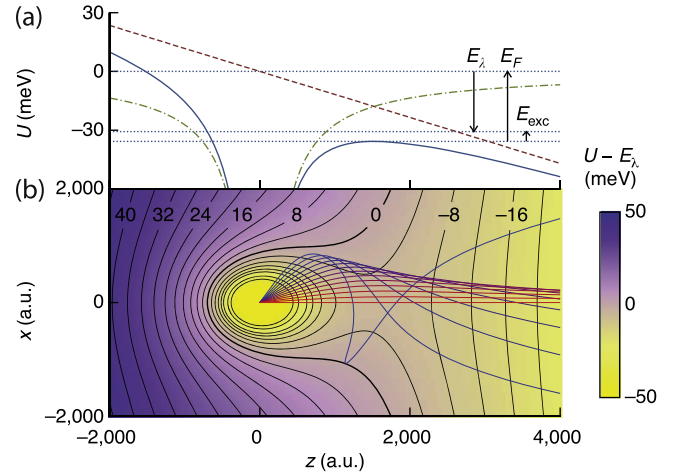


**Figure 7.** (a) Combined Coulomb–Stark potential ( $U_{cs}$ -solid curve), and separate Coulomb (dash–dot) and Stark (dashed) potentials. Potential landscapes with equipotential lines (black) and electron trajectories for varying initial emission angle. These show the transverse collimation of the electrons due to the saddle point, leading to a reduction in transverse momentum spread and therefore an increase in transverse emittance. Adapted with permission from [45].

atoms using only an ultrafast laser, the necessarily large laser frequency bandwidth would result in a large energy spread of the electrons produced. However, the anisotropic potential provided by the electric field permits exchange of energy between the transverse and longitudinal velocity components. Consequently, simultaneously cold and ultrafast bunches can be created [72, 73], with the transverse temperature reduction coming at the cost of an increased longitudinal beam temperature. The longitudinal energy spread is currently not a limiting factor for applications such as UED.

The original CAES proposal suggested exciting atoms to Rydberg states in a null-field [61] and then pulsed field ionisation. This method accesses higher coupling strengths due to excitation to definite Rydberg states rather than to the Stark-shifted ionisation continuum, and therefore a reduction in laser power required. Also, by pulsing the electric field very quickly ( $< 1$  ns) to a field strength much greater than that required for the ionisation of the Rydberg atoms, bunch compression can be obtained. Electrons produced later in the process will acquire more energy from the electric field than those liberated initially, resulting in the bunch becoming temporally compressed after it leaves the accelerator region. Work towards developing such a fast, high-voltage switch [69] showed that switching of 30 kV pulses with a rise time of 30 ns should produce bunches with a length of 80 ps. Ionisation of the excited Rydberg atoms can also occur without an electric field pulse via spontaneous avalanche ionisation, where blackbody photoionisation and ionising collisions lead to an accumulation of charge, followed by rapid electron-Rydberg collisions once a critical amount of charge has built up. Avalanche ionisation has been observed experimentally, with the process occurring over a number of microseconds [95].

A useful property of a CAES that, to date, remains unexplored is the ability to produce spin polarised electrons. An overview of the creation and uses of spin polarised sources is given in references [96, 97]. Spin polarised electrons are of interest for magnetoelectronics [98], fundamental tests of quantum mechanics [99] and for spin polarised microscopy [100]. Spin polarised microscopy can extract high resolution real-space information and, due to the magnetic sensitivity of the electrons, can provide additional magnetic information, such as magnetic domain structure [101].

High current pure sources of polarised electrons are not common. Using a negative electron affinity GaAs photocathode, an experimental purity of 43% is possible [102]. Polarised beams of up to 86% purity have been produced from GaAs/GaAs<sub>1-x</sub>P<sub>x</sub> photocathodes, however the efficiency of production is approximately 1% [103]. Trapped cold atoms provide a high level of control over the internal state of the atom. Techniques such as optical pumping [104] in conjunction with control over the polarisation of the light used for photoionisation should provide a way to efficiently produce high purity spin polarised electrons beams without any kind of separation.

### 3.2. Heating effects

The dynamics of electron detachment from the potential of a parent ion is important for understanding the velocity spread for a single-particle source. A CAES, however, typically involves ionising an atomic ensemble and the velocity spread is not then determined solely by the ionisation process. Additional heating can arise from the interactions between electrons and ions, as well as the interaction between neutral atoms and the plasma-like charge cloud. These heating processes can be understood by considering the charge cloud as a plasma. Here we briefly review the core theory of cold plasmas and their connection to a CAES.

In a null electric field, photoionisation of cold atoms can produce plasmas with temperatures in the range of 1–1000 K [105]. The charge cloud can be in the regime where the Coulomb interaction between charged particles is *greater* than the thermal energy, resulting in a *strongly coupled* plasma [106]. The strength of the coupling is quantified through the Coulomb coupling parameter

$$\Gamma = \frac{e^2}{4\pi\epsilon_0 a k_B T}, \quad (16)$$

where  $\epsilon_0$  is the permittivity of free space,  $k_B$  is the Boltzmann constant,  $T$  is the plasma temperature and  $a$  the Wigner–Seitz radius for particle density  $\rho$ :

$$a = \left[ \frac{3}{4\pi\rho} \right]^{1/3}. \quad (17)$$

For  $\Gamma > 1$  a plasma is strongly coupled and the traditional concepts used to explain the behaviour of plasmas, such as Debye screening and magnetohydrodynamics, are not valid. Extensive theoretical and computational investigations have been performed to better understand the dynamics of such a system [107–112]. Complications arise because immediately

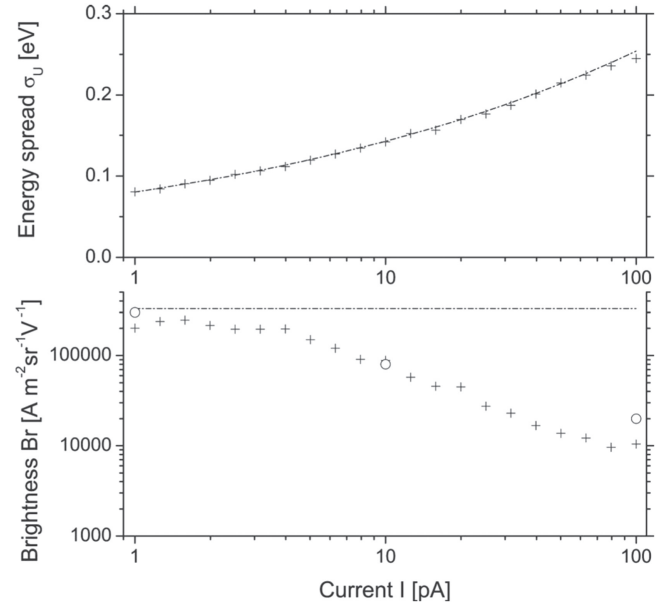


**Figure 8.** Particle tracking simulations showing the effect of disorder-induced heating on a cold ion beam. Crosses: simulated rms energy spread (top) and reduced brightness (bottom) as a function of current; open circles: reduced brightness calculated using transverse beam temperatures; and dash-dotted lines: fundamental limits. Adapted with permission from [115]. Copyright 2007, American Institute of Physics.

following photoionisation the system is far from equilibrium. Due to the non-ordered distribution of electrons and ions in the charge cloud, there is a random potential between the particles that is converted to varying kinetic energy in a process known as disorder-induced heating (DIH) [108, 111], reducing the quality of electron bunches [113, 114].

DIH is normally not apparent for conventional charged particle sources because DIH is negligible compared to thermal diffusion. For a CAES, it is the initial atomic temperature that is negligible and DIH dominates. A good illustration of the effect of DIH was provided by van der Geer *et al* [115] when they performed charge-particle tracking simulations for a cold atom ion source and showed that, as the bunch current increases, the brightness decreases due to the extra energy spread from DIH. Calculations of the minimum focused spot size achievable with the system increased from 0.8 nm with 1 pA current to 9.6 nm with 100 pA (figure 8).

To overcome DIH we need to provide spatial ordering within the system [116] to create a uniform Coulomb potential. There are many approaches that might achieve this, for instance, by providing structure with an optical lattice [117], or making use of atomic correlations in a degenerate Fermi gas [118]. Both of these techniques are, however, experimentally difficult, as all sites in a lattice must have exactly one particle, while Fermi degeneracy requires a very high atomic density  $\rho_a \approx 10^{19} \text{ m}^{-3}$ . Another method involves using the phenomena of ‘Rydberg blockade’, where an atom excited to a high-lying internal state inhibits other neighbouring atoms from also being excited. A pair of Rydberg atoms in a low angular momentum state (i.e.,  $S_{1/2}$ ) with

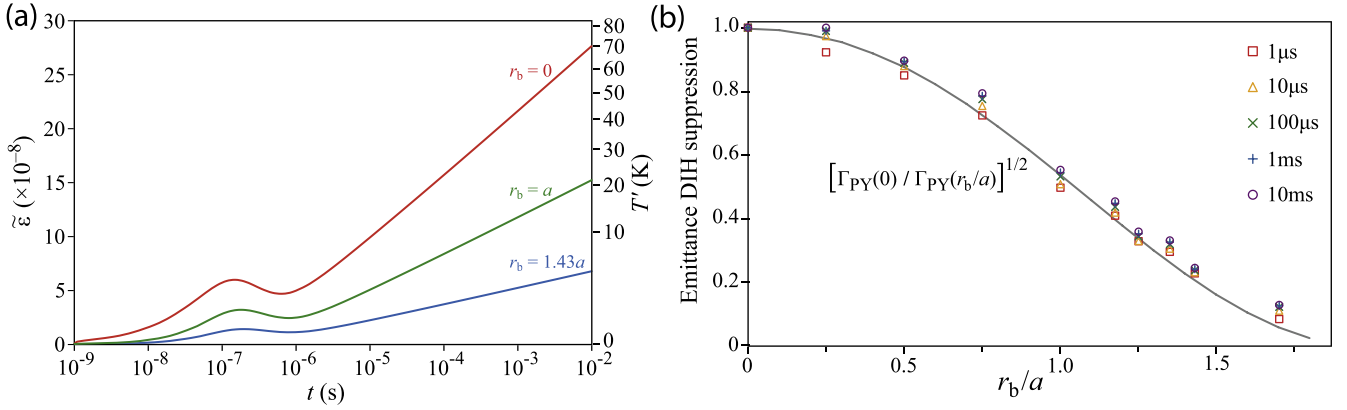


**Figure 9.** (a) Molecular dynamics simulations of dimensionless emittance and temperature growth caused by disordered-induced heating in a freely expanding  $^{85}\text{Rb}^+$  ion bunch with different amounts of order determined by the ratio of blockade radius  $r_b$  to the Wigner-Seitz radius  $a$ . (b) Simulations (points) and theory (line) for final emittance suppression as a function of  $r_b/a$  for a variety of expansion times. Adapted with permission from [125]. © American Physical Society.

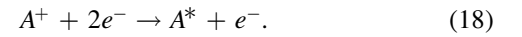
separation  $r$  interact, to leading order, via the van der Waals potential  $V(r) = C_6/r^6$  [119]. In an ensemble of atoms exposed to radiation coupling a ground state to a Rydberg state, with power-broadened linewidth  $\nu$ , the van der Waals interaction suppresses excitation of any ground-state atom within the blockade radius  $r_b = |C_6/\nu|^{1/6}$  of a Rydberg atom. For a  $^{85}\text{Rb}$  MOT with a typical atomic density of  $\rho_a = 10^{16} \text{ m}^{-3}$ , as  $n \rightarrow 100$ ,  $r_b \rightarrow 10 \text{ } \mu\text{m}$ , larger than the average inter-particle spacing quantified by the Wigner-Seitz radius. Excitation to Rydberg states in such a system will therefore lead to an increase in the spatial ordering of the particles, as demonstrated in a number of experiments [120–123]. The spatial ordering, or reduction in variation of atomic separation, will increase with the ratio of  $r_b/a$ .

The Coulomb coupling parameter  $\Gamma$  will also increase as the order increases and the temperature correspondingly decreases (equation (16)). DIH is then not only a hindrance for cold electron creation from a CAES, but also for the creation of a strongly-coupled ultracold plasma. Bannasch *et al* [124] proposed using Rydberg blockade to create a UCP. Their simulations compared direct coupling from the ground state to the ionisation threshold against excitation from the ground state to a Rydberg state, followed by ionisation. They showed that the ion temperature in the UCP dropped from 1 K down to under 100 mK due to the increase in order provided by Rydberg blockade.

In non-neutral charged particle bunches there will be competition between the effects of DIH and adiabatic cooling, which prevents thermal equilibration at any point during the expansion [126, 127]. Murphy *et al* [125] investigated the effect of increased order created via Rydberg blockade. Figure 9 shows the result of numerical simulations, with a reduction in emittance in an expanding uniform ellipsoidal ion bunch linked to an increase in order up to  $r_b = 1.7a$ , the hard-sphere packing limit. To date, blockade experiments have reported  $r_b/a$  up to 1.2 [95], which would correspond to an emittance reduction of 0.4, leading to a six-fold increase in beam brightness. Creating bunches with higher blockade parameters may be possible through variation of the laser

frequency and intensity during the Rydberg excitation and photoionisation process [128, 129], Rydberg excitation of atoms in an optical lattice with high filling fraction [130], or by ionisation of atoms in spatially tailored micro trap arrays [131].

Another effect which results in plasma heating is three-body recombination (TBR), whereby an ion interacts with two electrons to form an excited atom and an energetic electron,



The TBR rate  $R_{\text{TBR}}$  displays the form [132]

$$R_{\text{TBR}} \propto T^{-9/2}, \quad (19)$$

and at low temperatures TBR can become the dominant heating mechanism on short time scales. Such recombination dynamics are analogous to dynamics in globular clusters [133], proving a unique platform for the study of stellar dynamics on the laboratory scale. The heating time  $\tau_t$  that characterises the time for thermal equilibration to be established within the plasma is given by

$$\tau_t = \frac{a}{\sqrt{e^2/4\pi\epsilon_0 a m_{e,i}}} \quad (20)$$

where  $m_{e,i}$  are the electron and parent ion mass. Equation (20) is identified as the inverse of the plasma frequency  $\omega_p$

$$\omega_p = \frac{1}{\tau_t} = \frac{1}{a} \sqrt{\frac{e^2}{4\pi\epsilon_0 a m_{e,i}}}. \quad (21)$$

The time scale for the heating will, therefore, be density dependent and different for electrons and ions. For densities typically achieved in a CAES, the time taken for electron/ion equilibration is of order nanoseconds/microseconds. Collective plasma heating effects are less important for slow ionisation schemes in a CAES because when ionisation occurs in a static electric field, the ion and electron are accelerated in opposite directions. However, for ultrafast ionisation schemes, collective plasma heating effects will be important.

The effects of plasma heating in combination with the single particle ionisation dynamics will determine the initial temperature of the electron beam, but the final electron beam temperature is then further subject to the influence of Coulomb interactions within the beam.

### 3.3. Space-charge expansion and electron bunch shaping

Coulomb interactions within electron bunches can lead to degradation of the emittance and brightness. This degradation manifests itself through two main effects: the microscopic statistical Coulomb effect (discussed in section 3.2) and macroscopic Coulomb expansion, also known as space-charge expansion. Space-charge expansion is a critical issue for applications in electron and ion microscopy [134, 135], high-energy particle accelerator injection [136], and, of particular interest here, UED [38, 137, 138]. The transverse emittance and brightness degrade as the bunch charge increases, and also the temporal bunch width will increase, limiting the temporal resolution [80, 139–141].

As discussed in section 2.2, single-shot UED requires that each electron bunch contains enough charge to produce a measurable diffraction pattern, coupled with pulse durations of hundreds of femtoseconds. In combination, these requirements lead to charge densities which will exhibit severe Coulomb explosion. One might therefore come to the conclusion that space-charge expansion would limit the ability of UED to perform single-shot experiments. However, space-charge expansion itself is not the problem, rather it is the *reversibility* of the expansion that limits the minimum focal sizes, in both the transverse and longitudinal directions. Put another way, if the space-charge-induced growth is linear (the bunch maintains its shape while its size increases) then linear electron-optics can be used to focus the bunch back to its initial size with no increase in emittance. These criteria are satisfied [143, 144] by a uniform density three-dimensional (3D) ellipsoid with transverse radii  $r_x$ ,  $r_y$ , and longitudinal radius  $r_z$  such that the confinement surface is given by

$$\left(\frac{x}{r_x}\right)^2 + \left(\frac{y}{r_y}\right)^2 + \left(\frac{z}{r_z}\right)^2 = 1. \quad (22)$$

For bunches with an ellipsoidal profile, transverse beam growth can be reversed using conventional linear electron-optical elements, but longitudinal growth must be reversed with a nonlinear optical element. For example, a microwave cavity operating with a  $TEM_{010}$  field can be used to impose a time-dependent potential to an electron bunch [145]. The phase of the microwave wavefield is controlled to impart a greater momentum kick to the slower electrons at the tail of the bunch and a small kick to the fastest electrons at the front of the bunch, leading to a focusing of the bunch in a particular plane in  $z$ . Van Oudheusden *et al* used this technique to compress a 10 ps bunch to a sub-100 fs bunch, with sufficient bunch charge to collect a diffraction image from gold [147]. The electron pulse length can be reduced by removing electrons outside a particular energy range, but the current is then

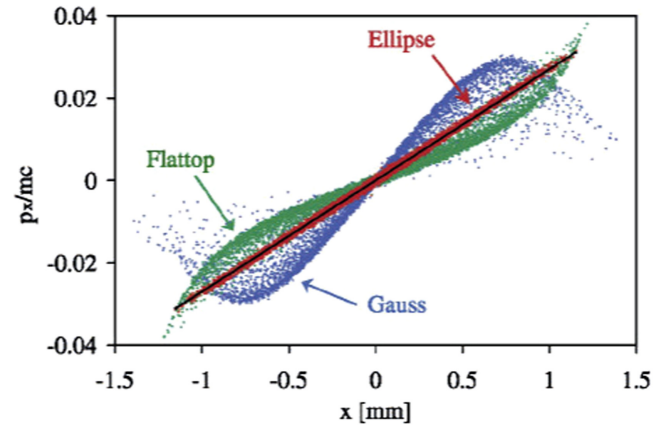


**Figure 10.** Particle-tracking simulations of the phase-space distributions of three different initial transverse excitation profiles (dots), as well as theoretical ‘pancake’ profile (line) following space-charge expansion. Note the linearity of the ellipsoidal profile, indicating shape preservation and therefore reversibility of the expansion. Adapted with permission from [142]. © American Physical Society.

also reduced. For example, Tokita *et al* [146] created a 500 fs pulse by magnetically selecting the 350 keV component from a pulse with a 1 MeV energy spread. The bunch charge was sufficient to collect a single-shot diffraction image from gold, but large increases in brightness are required for diffraction imaging of weakly scattering objects such as biological samples, and thus methods which do not reduce the beam current are preferred.

Figure 10 shows the difference in the phase-space distribution between linear space-charge expansion for an ellipsoid compared to two other common transverse density distributions: a flattop and a Gaussian. For the ellipse, the relationship between the particle velocity and position remains linear, while for the Gaussian the velocity/position slope is steeper closer to the bunch centre than at the edge due to its higher central density, and the opposite is true for the flattop. The altering of the effective phase-space profile of the Gaussian and flattop distributions leads to an increase in emittance, and therefore a decrease in their focusability.

Ellipsoidal electron distributions have been produced from photo-cathode-based sources. For instance, using spatial and temporal pulse shaping of the laser beam, a uniform ellipsoid can be directly created from a photo-cathode surface [148, 149]. An alternate technique, initially proposed by Serafini [150, 151] and then refined by Luiten *et al* [142], uses transverse shaping to create a semicircular distribution with  $r_x = r_y = R$  and a very short  $z$  profile ( $\sigma_z \ll R$ ). The high-density two-dimensional bunches expand rapidly in the direction of propagation ( $z$ ) due to the initially large space-charge forces, evolving into uniform ellipsoids. The method requires that the bunch creation time is short enough such that the longitudinal spread of the bunch due to the accelerator is negligible, and also that the space-charge field strength that develops during bunch creation remain much smaller than the acceleration field strength. The second condition places a limit on the maximum charge of a uniform ellipsoid created

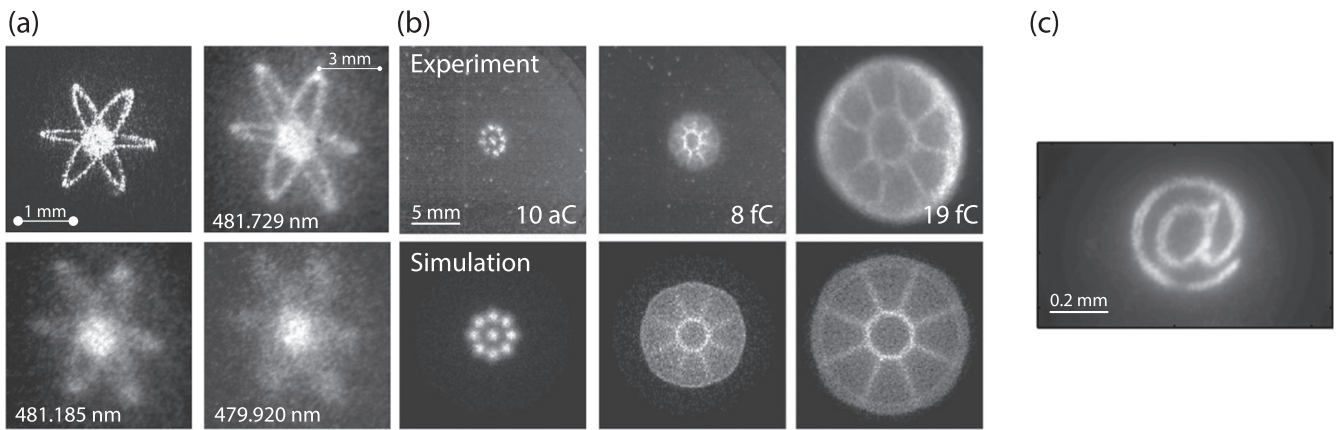


**Figure 11.** (a) Excitation-laser intensity profile (top left), and sequence of detected electron bunches extracted with varying excess ionisation energies. Adapted with permission from [62]. (b) Investigating space-charge interactions between ion bunches via bunch shaping, showing increased expansion and the emergence of high-density regions due to intra-beam space-charge effects. Adapted with permission from [15]. (c) Complex ion beam pattern demonstrating the ability of bunch shaping using an iterative Fourier transform algorithm. Adapted from [155]; used in accordance with the Creative Commons Attribution (CC BY) licence.

using this method, for a given radius. For the purposes of single-shot UED experiments, a bunch charge of  $10^6$  electrons created with a  $\sigma_t \approx 100$  fs laser pulse, an electric field of  $100 \text{ keV cm}^{-1}$ , and  $R \approx 100 \text{ } \mu\text{m}$  (see table 1) satisfy both conditions. The pancake scheme was first demonstrated, and then characterised, by the group of Musumeci *et al* [152, 153], where 35 fs (rms) ultraviolet pulses were used to illuminate a metallic photocathode inside a photoelectron gun for a bunch charge of 15 pC with transverse beam shaping provided by an iris with a radius of approximately the same size as the laser beam width. In 2013, Piot *et al* demonstrated a twenty-fold increase in bunch charge up to 500 pC using the same method with an L-band rf photoinjector [154]. Uniform ellipsoidal bunches can also be created with  $\sigma_z \gg R$  with a parabolic longitudinal charge density distribution [79]. These so-called ‘cigar’ bunches experience much smaller space-charge forces and therefore lower emittance and higher brightness, but will have larger relative energy spread and temporal profiles.

For a CAES using two-photon excitation, dynamic 3D shaping is readily accessible using spatial-light modulators (SLMs). The first demonstration of shaping with a cold atom source used the transverse spread of an electron bunch from an initially well-defined distribution to measure the temperature of the liberated electrons as a function of the ionisation laser wavelength (figure 11(a)) [62]. Shaping of the initial particle distribution has also been used to measure the coherence length of the electrons at the source [19] and, with ion bunches, to investigate complex space-charge effects without the loss of detail normally expected due to thermal diffusion [15] (figure 11(b)). The bunch sizes in these experiments were all of order of millimetres. Bunch shaping in a CAES using an iterative Fourier transform algorithm has recently achieved resolution on the order of  $10 \text{ } \mu\text{m}$ , limited by the SLM pixel size (figure 11(c)) [155].

#### 4. Cold atom electron diffraction

In 2014, van Mourik *et al* [71] from the Eindhoven group were the first to demonstrate UED with a CAES. As discussed in section 3, in the Eindhoven CAES  $^{85}\text{Rb}$  atoms are first excited to the  $5P$  state, followed by ionisation via a 100 fs pulsed laser beam perpendicular to the excitation laser. This results in a few hundred electrons per pulse being emitted from an ionisation region with initial rms sizes  $\sigma_o = 30$  (50)  $\mu\text{m}$  in the  $x$  ( $y$ ) directions. As shown in figure 12(a), the electron bunches were accelerated to an energy of over 10 keV before being collimated and then focused onto a graphite sample with a pair of magnetic lenses, and detected on an MCP at 30 cm free-space propagation distance. Figure 12(b) shows the diffraction pattern, with (i) diffraction patterns focused onto the MCP, (ii) and (iii) diffraction patterns produced with focusing onto the sample with electron temperatures of 10 K and 250 K respectively. The different widths of the diffraction spots between (b)(ii) and (b)(iii) are a good illustration of the importance of low electron temperatures for improved image resolution. The different temperatures were achieved by varying the wavelength of the ionisation laser (equation (14)). All diffraction patterns shown in figure 12(b) were achieved by combining approximately 1,000 individual images.

The first single-shot diffraction experiment with a CAES [74] also used  $^{85}\text{Rb}$  and first exciting to the  $5P$  state, followed by ionisation with a 5 ns 480 nm pulsed laser. By using a much larger ionisation volume ( $\sigma_o = 425 \text{ } \mu\text{m}$ ) a bunch charge of approximately 500 000 electrons was produced. The extracted electrons were accelerated to an energy of 8 keV before being focused through a sample of gold foil towards the detector with a single magnetic lens. The large bunch charge achieved allowed for sufficient signal per shot to obtain useful diffraction data. An example of single-shot diffraction is shown in figure 13(a). The high signal-to-noise ratio for individual shots allowed for automatic registering of individual images to account for jitter in the electron

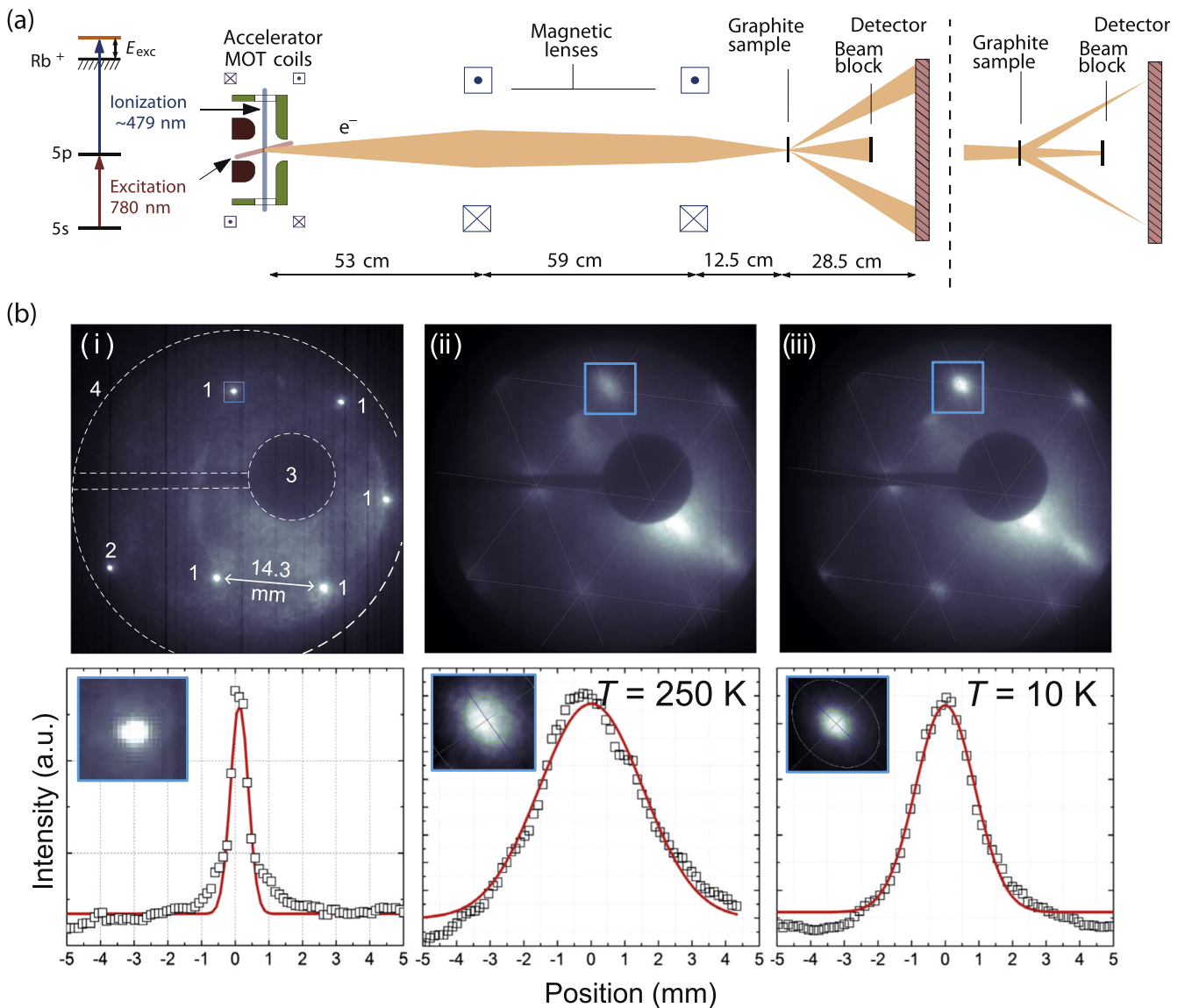


**Figure 12.** (a) Cold atom electron source diffraction set-up. (b) Ultrafast diffraction images from a 13–20 nm thick mono crystalline sample on a 200 mesh copper TEM grid with 10–13 keV electrons for: (i) focusing at the detector plane; (ii) focusing at the sample plane with  $T = 250$  K electrons; and (iii) focusing at the sample plane with  $T = 10$  K electrons. Diffraction images achieved by combining approximately 1,000 individual images. Adapted from [71]; used in accordance with the Creative Commons Attribution (CC BY) licence.

bunch trajectory (due mainly to decaying MOT magnetic fields). An average of 2,000 registered images is shown in figure 13(b) and a comparison of single-shot, registered- and direct-averages is shown for a lineout of an individual Bragg reflection in figure 13(c). This final image illustrates the importance of being able to produce single-shot images, with the single-shot and registered-average images both showing a higher peak intensity and narrower widths. Single-shot reflection high-energy electron diffraction (RHEED) was also demonstrated, for diffraction from a wafer of mono crystalline silicon. RHEED is an important technique because high quality single crystals are more readily available as bulk wafers than nanometer-thick foils, and bulk wafers are too thick for transmission at typical CAES electron energies.

Table 1 compares the properties of cold atom and thermal sources that have achieved few- and single-shot UED. The thermal sources used lasers with pulse widths on the order of 100 fs incident on a photocathode to produce electron bunches with durations less than 600 fs. The single-shot diffraction results [36, 41–43] were obtained from gold foil, using between  $4 \times 10^5$  and  $10^7$  electrons per bunch. Some of the measurements used an aperture to increase bunch coherence at the expense of current. One advantage of the CAES over thermal sources is that aperturing of the beam is not required, with all electrons in a bunch focused through the sample, thereby reducing the required single-shot source current and related space-charge expansion.

CAES experiments have, to date, only been demonstrated for electron energies around 10 keV. While there is no

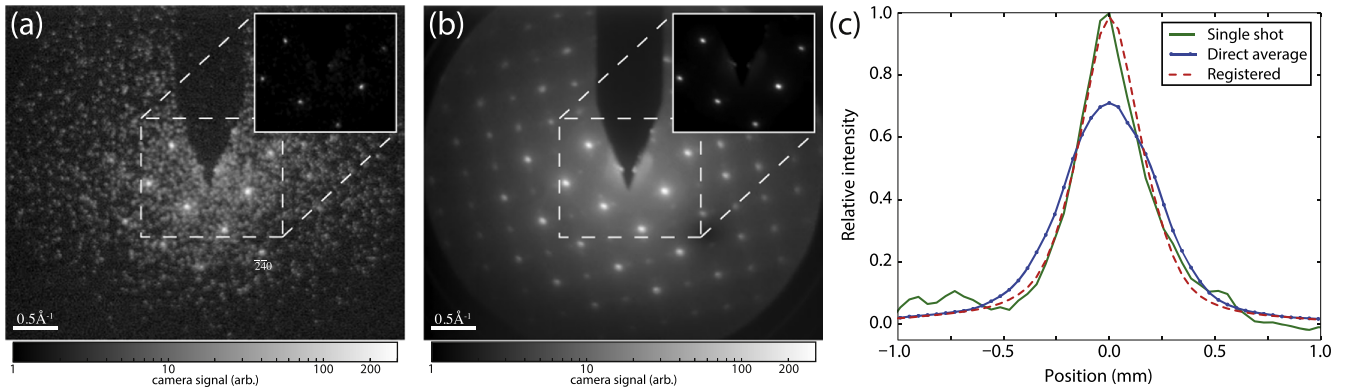


**Figure 13.** (a) Single-shot diffraction pattern achieved with a 5 ns 8 keV electron bunch from a 11 nm thick gold foil mounted on a 3 mm TEM grid. (b) Registered average of 2,000 individual images. (c) A lineout of the  $(\bar{2}00)$  Bragg reflection, showing the difference between single-shot, registered average and direct averages in term of peak intensity and width. For (a) and (b) the main image is logarithmically scaled, inset is linearly scaled. Adapted from [74].

theoretical limitation to the maximum bunch energy in a CAES, increasing the electric field strength  $F$  to increase the energy will lead to an increase in the bunch energy spread as described in equation (15), though the fractional energy spread will not increase. For the system used in reference [74], with a 5 cm gap between accelerator plates and an ionisation laser  $\sigma_z = 15 \mu\text{m}$ , the fractional energy spread is 0.01%. This compares favourably to a typical RF photosource [43] where the energy spread was measured as 0.5% [156]. Decreasing the laser width will reduce the energy spread but, for the same transverse emittance, will also reduce the bunch charge as the ionisation volume is reduced.

Space-charge effects can be avoided in single-shot diffraction experiments by moving to higher energies (MeV) [42, 43]. Another way of reducing space-charge effects is to use lower energies and an initially longer bunch, but then to compress it using a radio-frequency (RF) cavity. A bunch that had expanded under space-charge effects to an rms length of 10 ps was compressed to under 100fs [12, 36]. A secondary accelerator can be used to increase the bunch energy without increasing the energy spread, thus enabling a 100 keV electron source with 0.001% energy spread. Reducing the energy spread is important to reduce chromatic aberration effects.

To compare the relative transverse coherence lengths of the sources ( $C_\perp$ , equation (8)), we must determine both the initial temperature and transverse size of the initial bunches. For a nano-second CAES, where  $T \approx 10 \text{ K}$  and therefore  $L_\perp \approx 10 \text{ nm}$  [19],  $C_\perp = 2 \times 10^{-4}$  [70, 71]. It has been found that, for femtosecond excitation, this value does not increase despite the increased energy spread of the excitation laser because the reduction in the electron transverse velocity is reduced by the Coulomb-Stark potential [45]. As can be seen from table 1,  $C_\perp = 10^{-6}$ – $10^{-5}$  for most photocathode sources due to their high temperature ( $T \approx 1,000 \text{ K}$ ). To obtain single-shot UED from, for instance, protein microcrystals will require  $10^6$  electrons with  $C_\perp$  between  $10^{-5}$  and  $10^{-3}$  [12, 44, 45]. As space-charge expansion will play a large role, we assume the creation of a uniform ellipsoidal bunch, as discussed in equation (3.3), to ensure maximum bunch compression and minimum emittance. This requires an

ellipsoid transverse radius  $R \ll \sigma_z$ . The lower limit of  $C_\perp$  is easily obtainable for a CAES with  $\sigma_o = 1 \text{ mm}$  and  $\sigma_z = 15 \mu\text{m}$  for an atomic density  $\rho_a = 10^{16} \text{ m}^{-3}$ , assuming 50% ionisation efficiency. Achieving  $C_\perp = 10^{-3}$  is a much more difficult proposition. We would require  $\sigma_o = 10 \mu\text{m}$  and therefore  $\sigma_z \approx 1 \mu\text{m}$ . In this case, even assuming 100% ionisation efficiency, an atomic density of  $\rho_a = 10^{20} \text{ m}^{-3}$  is needed, well above the quantum degeneracy limit for 100  $\mu\text{K}$  electrons ( $\rho_e \approx 10^{17} \text{ atoms m}^{-3}$ ). To reduce the required density, a cigar bunch could be used (i.e., with  $\sigma_z \gg R$ ) which would result in a proportionally larger energy spread and longer bunch length. Energy spread is not currently a limiting factor in diffraction experiments, while the effects of increased bunch duration can be mitigated with a greater beam energy, offering a pathway to obtain electron pulses with  $C_\perp = 10^{-3}$ .

## 5. Summary and outlook

Cold electron sources offer unique properties with the potential for significant impact, particularly in relation to imaging at atomic spatial and temporal scales. They can be ultrafast, very low in energy dispersion, and the peak brightness is competitive with many conventional sources. They have broad emission area, but also high transverse coherence at the origin, orders of magnitude greater than other bright sources. These characteristics lend themselves to diffractive imaging, in particular conventional UED based on crystallographic approaches, and also to ultrafast CDI.

CDI is a relatively new form of lensless high-resolution imaging which can be used for imaging non-repeated (non-crystalline) materials [157]. The development of CDI has been driven by the possibility of single molecule imaging with XFELs, but is also now seeing a range of applications in synchrotron-based high-resolution x-ray imaging. More recently, CDI is attracting interest for electron imaging with atomic resolution using modern aberration-corrected microscopes where transverse coherence is of order 0.3 nm [13]. The intrinsic coherence length of a CAES is of order 10 nm, and detailed knowledge of the partial coherence properties of

the source [19, 158] can be incorporated into the image reconstruction to make the recovery more robust [159]. The order-of-magnitude greater transverse coherence of cold-atom sources, the ability to shape the bunches to control Coulomb explosion, and access to many established cooling and trapping techniques and Rydberg ionisation mechanisms to suppress DIH all promise exciting advances in ultrafast electron CDI and possibly cryo transmission electron microscopy [9–11]. With cold ion sources rapidly approaching commercial availability [160] there is every reason to expect similar exciting progress with CAESs in the near future.

## Acknowledgments

BMS gratefully acknowledges the support of a University of Melbourne McKenzie Fellowship. This work was supported by the Australian Research Council Discovery Project DP140102102.

## References

- [1] Hentschel M *et al* 2001 *Nature* **414** 509
- [2] Baker S, Robinson J, Haworth C, Teng H, Smith R, Chirilă C, Lein M, Tisch J and Marangos J 2006 *Science* **312** 424
- [3] Cavalieri A *et al* 2007 *Nature* **449** 1029
- [4] Uiberacker M *et al* 2007 *Nature* **446** 627
- [5] Dantus M, Bowman R and Zewail A 1990 *Nature* **343** 737–9
- [6] Quiney H M and Nugent K A 2011 *Nat. Phys.* **7** 142
- [7] Seibert M M *et al* 2011 *Nature* **470** 78
- [8] Ayyer K *et al* 2016 *Nature* **530** 202–6
- [9] Wang R Y R, Kudryashev M, Li X, Egelman E H, Basler M, Cheng Y, Baker D and DiMaio F 2015 *Nat. Methods* **12** 335–8
- [10] Callaway E 2015 *Nature* **525** 172
- [11] Milne J L, Borgnia M J, Bartesaghi A, Tran E E, Earl L A, Schauder D M, Lengyel J, Pierson J, Patwardhan A and Subramaniam S 2013 *FEBS J.* **280** 28–45
- [12] van Oudheusden T, de Jong E F, van der Geer S B, 't Root W P E M O, Luiten O J and Siwick B J 2007 *J. Appl. Phys.* **102** 093501
- [13] Putkunz C T *et al* 2012 *Phys. Rev. Lett.* **108** 073901
- [14] Zhu Y and Dürr H 2015 *Phys. Today* **68** 32
- [15] Murphy B F *et al* 2014 *Nat. Commun.* **5** 4281
- [16] McClelland J J, Steele A V, Knuffman B, Twedt K A, Schwarzkopf A and Wilson T M 2014 *Appl. Phys. Rev.* **3** 011302
- [17] Humphries S 1990 *Charged Particle Beams* (New York: Wiley)
- [18] Hawkes P W and Kasper E 1996 *Principles of Electron Optics II: Applied Geometrical Optics* (London: Academic)
- [19] Saliba S D, Putkunz C T, Sheludko D V, McCulloch A J, Nugent K A and Scholten R E 2012 *Opt. Express* **20** 3967–74
- [20] Van Cittert P 1934 *Physica* **1** 201–10
- [21] Engelen W J, Smakman E P, Bakker D J, Luiten O J and Vredendregt E J D 2013 *Ultramicroscopy* **136** 73
- [22] Williams G, Quiney H, Peele A and Nugent K 2007 *Phys. Rev. B* **75** 104102
- [23] Saliba S D, Putkunz C T, Sheludko D V, McCulloch A J, Nugent K A and Scholten R E 2012 *Opt. Express* **20** 3967–74
- [24] Schoenlein R W, Leemans W P, Chin A H, Volfbeyn P, Glover T E, Balling P, Zolotorev M, Kim K, Chattopadhyay S and Shank C V 1996 *Science* **274** 236
- [25] Kondratenko A M and Saldin E L 1980 *Part. Accel.* **10** 207 ([https://inis.iaea.org/search/search.aspx?orig\\_q=RN:12582046](https://inis.iaea.org/search/search.aspx?orig_q=RN:12582046))
- [26] Derbenev Y, Kondratenko A and Saldin E L 1982 *Nucl. Instrum. Methods* **193** 415
- [27] Murphy J B and Pellegrini C 1985 *Nucl. Instrum. Methods A* **237** 159
- [28] Ackermann W *et al* 2007 *Nat. Photon.* **1** 336
- [29] Emma P *et al* 2010 *Nat. Photon.* **4** 641
- [30] Singer A *et al* 2012 *Opt. Express* **20** 17480
- [31] Chapman H N *et al* 2006 *Nat. Phys.* **2** 839–43
- [32] Chapman H N *et al* 2011 *Nature* **470** 73–7
- [33] Boutet S *et al* 2012 *Science* **74** 10
- [34] Kimura T *et al* 2014 *Nat. Commun.* **5** 3052
- [35] Kupitz C *et al* 2014 *Nature* **513** 261
- [36] van Oudheusden T, Pasmans P L E M, van der Geer S B, de Loos M J, van der Wiel M J and Luiten O J 2010 *Phys. Rev. Lett.* **105** 264801
- [37] Sciaini G and Miller R J D 2011 *Rep. Prog. Phys.* **74** 096101
- [38] Siwick B J, Dwyer J R, Jordan R E, Miller R J D, Dwyer R S, Jordan R E and Miller R J D 2003 *Science* **302** 1382
- [39] Harb M, Ernstorfer R, Hebeisen C T, Sciaini G, Peng W, Dartigalongue T, Eriksson M A, Lagally M G, Kruglik S G and Miller R J D 2008 *Phys. Rev. Lett.* **100** 155504
- [40] Sciaini G, Harb M, Kruglik S G, Payer T, Hebeisen C T, Heringdorf F J M Z, Yamaguchi M, Hoegen M H V, Ernstorfer R and Miller R J D 2009 *Nature* **458** 56
- [41] Tokita S, Inoue S, Masuno S, Hashida M and Sakabe S 2009 *Appl. Phys. Lett.* **95** 111911
- [42] Li R *et al* 2010 *Rev. Sci. Instrum.* **81** 036110
- [43] Musumeci P, Moody J T, Scooby C M, Gutierrez M S, Bender H A and Wilcox N S 2010 *Rev. Sci. Instrum.* **81** 013306
- [44] van der Geer S B, de Loos M J, Vredendregt E J D and Luiten O J 2009 *Microsc. Microanal.* **15** 282–9
- [45] Engelen W J, van der Heijden M A, Bakker D J, Vredendregt E J D and Luiten O J 2013 *Nat. Commun.* **4** 1693
- [46] de Jonge N, Allioux M, Oostveen J, Teo K and Milne W 2005 *Phys. Rev. Lett.* **94** 186807
- [47] Pascale-Hamri A, Perisanu S, Derouet A, Journet C, Vincent P, Ayari A and Purcell S 2014 *Phys. Rev. Lett.* **112** 126805
- [48] Schwind G A, Magera G and Swanson L W 2006 *J. Vac. Sci. Technol. B* **24** 2897
- [49] Zhang H, Tang J, Yuan J, Yamauchi Y, Suzuki T T, Shinya N, Nakajima K and Qin L C 2015 *Nat. Nanotechnol.* **11** 273–9
- [50] Chang C C, Kuo H S, Hwang I S and Tsong T T 2009 *Nanotechnology* **20** 115401
- [51] Oshima C, Rokuta E, Itagaki T, Ishikawa T, Cho B, Kuo H S, Hwang I S and Tsong T T 2005 *e-J. Surf. Sci. Nanotechnol.* **3** 412
- [52] Orloff J 2008 *Handbook of Charged Particle Optics* (Boca Raton, FL: CRC)
- [53] Cultrera L, Karkare S, Lee H, Liu X, Bazarov I and Dunham B 2015 *Phys. Rev. ST Accel. Beams* **18** 113401
- [54] Wineland D J and Itano W M 1979 *Phys. Rev. A* **20** 1521
- [55] Ertmer W, Blatt R, Hall J and Zhu M 1985 *Phys. Rev. Lett.* **54** 996
- [56] Phillips W D, Prodan J V and Metcalf H J 1985 *J. Opt. Soc. Am. B* **2** 1751–67
- [57] Aspect A, Arimondo E, Kaiser R E A, Vansteenkiste N and Cohen-Tannoudji C 1988 *Phys. Rev. Lett.* **61** 826

- [58] Metcalf H J and Van der Straten P 2012 *Laser Cooling and Trapping* (Berlin: Springer)
- [59] Flechard X, Nguyen H, Wells E, Ben-Itzhak I and DePaola B 2001 *Phys. Rev. Lett.* **87** 123203
- [60] Dörner R, Mergel V, Jagutzki O, Spielberger L, Ullrich J, Moshhammer R and Schmidt-Böcking H 2000 *Phys. Rep.* **330** 95–192
- [61] Claessens B J, van der Geer S B, Taban G, Vredendregt E J D and Luiten O J 2005 *Phys. Rev. Lett.* **95** 164801
- [62] McCulloch A J, Sheludko D V, Saliba S D, Bell S C, Junker M, Nugent K A and Scholten R E 2011 *Nat. Phys.* **7** 785
- [63] Xia G, Harvey M, Murray A J, Bellan L, Bertsche W, Appleby R B, Mete O and Chattopadhyay S 2014 *J. Instrum.* **9** P06011
- [64] Knuffman B, Steele A V and McClelland J J 2013 *J. Appl. Phys.* **114** 044303
- [65] Claessens B J, Reijnders M P, Taban G, Luiten O J and Vredendregt E J D 2007 *Phys. Plasmas* **14** 093101
- [66] Hanssen J L, Hill S B, Orloff J and McClelland J J 2008 *Nano Lett.* **8** 2844
- [67] Knuffman B, Steele A V, Orloff J and McClelland J J 2011 *New J. Phys.* **13** 103035
- [68] Debernardi N, van Vliembergen R W L, Engelen W J, Hermans K H M, Reijnders M P, van der Geer S B, Mutsaers P H A, Luiten O J and Vredendregt E J D 2012 *New J. Phys.* **14** 083011
- [69] Taban G, Reijnders M P, Bell S C, van der Geer S B, Luiten O J and Vredendregt E J D 2008 *Phys. Rev. Spec. Top.—Accel. Beams* **11** 050102
- [70] Taban G, Reijnders M P, Fleskens B, van der Geer S B, Luiten O J and Vredendregt E J D 2010 *Europhys. Lett.* **91** 46004
- [71] van Mourik M W, Engelen W J, Vredendregt E J D and Luiten O J 2014 *Struct. Dyn.* **1** 034302
- [72] Engelen W J, Vredendregt E J D and Luiten O J 2014 *Ultramicroscopy* **147** 61
- [73] McCulloch A J, Sheludko D V, Junker M and Scholten R E 2013 *Nat. Commun.* **4** 1692
- [74] Speirs R W, Putkunz C T, McCulloch A J, Nugent K A, Sparkes B M and Scholten R E 2015 *J. Phys. B: At. Mol. Opt. Phys.* **48** 214002
- [75] Harvey M and Murray A J 2008 *Phys. Rev. Lett.* **101** 173201
- [76] Kime L *et al* 2013 *Phys. Rev. A* **88** 033424
- [77] Wouters S H W, ten Haaf G, Notermans R P M J W, Debernardi N, Mutsaers P H A, Luiten O J and Vredendregt E J D 2014 *Phys. Rev. A* **90** 063817
- [78] ten Haaf G, Wouters S H W, van der Geer S B, Vredendregt E J D and Mutsaers P H A 2014 *J. Appl. Phys.* **116** 244301
- [79] Luiten O J, Claessens B J, van der Geer S B, Reijnders M P, Taban G and Vredendregt E J D 2007 *Int. J. Mod. Phys. A* **22** 3882–97
- [80] King W E, Campbell G H, Frank A, Reed B, Schmerge J F, Siwick B J, Stuart B C and Weber P M 2005 *J. Appl. Phys.* **97** 111101
- [81] Gahlmann A, Park S T and Zewail A H 2008 *Phys. Chem. Chem. Phys.* **10** 2894
- [82] van der Geer S, Vredendregt E, Luiten O and de Loos M 2014 *J. Phys. B: At. Mol. Opt. Phys.* **47** 234009
- [83] Javan A and Levine J 1972 *IEEE J. Quantum Electron.* **8** 827–32
- [84] Killian T, Kulin S, Bergeson S, Orozco L, Orzel C and Rolston S 1999 *Phys. Rev. Lett.* **83** 4776–9
- [85] Merkt F, Osterwalder A, Seiler R, Signorell R, Palm H, Schmutz H and Gunzinger R 1998 *J. Phys. B: At. Mol. Opt. Phys.* **31** 1705
- [86] Gallagher T 2005 *Rydberg Atoms* vol 3 (Cambridge: Cambridge University Press)
- [87] Gribakin G F and Kuchiev M Y 1997 *Phys. Rev. A* **55** 3760
- [88] Kondratovich V and Ostrovsky V 1984 *J. Phys. B: At. Mol. Opt. Phys.* **17** 1981
- [89] Blondel C, Delsart C and Dulieu F 1996 *Phys. Rev. Lett.* **77** 3755
- [90] Beletsky V 2001 *Essays on the Motion of Celestial Bodies* (Basel: Birkhäuser)
- [91] Zhao L and Delos J 2010 *Phys. Rev. A* **81** 053417
- [92] Zhao L and Delos J 2010 *Phys. Rev. A* **81** 053418
- [93] Zhao L, Xiao D and Fabrikant I 2015 *Phys. Rev. A* **91** 043405
- [94] Stodolna A, Rouzée A, Lépine F, Cohen S, Robicheaux F, Gijbsbertsen A, Jungmann J, Bordas C and Vrakking M 2013 *Phys. Rev. Lett.* **110** 213001
- [95] Robert-de Saint-Vincent M, Hofmann C S, Schempp H, Günter G, Whitlock S and Weidemüller M 2013 *Phys. Rev. Lett.* **110** 045004
- [96] Subashiev A, Mamaev Y, Yashin Y and Clendenin J 1999 *Phys. Low-Dim. Struct.* **1** 1–36
- [97] Kessler J 2013 *Polarized Electrons* 2nd edn (Berlin: Springer)
- [98] Fiederling R, Keim M, Reuscher G, Ossau W, Schmidt G, Waag A and Molenkamp L 1999 *Nature* **402** 787–90
- [99] Wiesendanger R, Güntherodt H, Güntherodt G, Gambino R and Ruf R 1990 *Phys. Rev. Lett.* **65** 247–50
- [100] Pierce D 1988 *Phys. Scr.* **38** 291
- [101] Koike K and Hayakawa K 1984 *Appl. Phys. Lett.* **45** 585
- [102] Pierce D, Celotta R, Wang G, Unertl W, Galejs A, Kuyatt C and Mielczarek S 1980 *Rev. Sci. Instrum.* **51** 478–99
- [103] Maruyama T *et al* 2004 *Appl. Phys. Lett.* **85** 2640–2
- [104] Happer W 1972 *Rev. Mod. Phys.* **44** 169–249
- [105] Killian T, Pattard T, Pohl T and Rost J 2007 *Phys. Rep.* **449** 77–130
- [106] Ichimaru S 1982 *Rev. Mod. Phys.* **54** 1017
- [107] Robicheaux F and Hanson J 2003 *Phys. Plasmas* **10** 2217
- [108] Kuzmin S and O’Neil T 2002 *Phys. Rev. Lett.* **88** 65003
- [109] Kuzmin S and O’Neil T 2002 *Phys. Plasmas* **9** 3743
- [110] Mazevet S, Collins L and Kress J 2002 *Phys. Rev. Lett.* **88** 55001
- [111] Murillo M 2001 *Phys. Rev. Lett.* **87** 115003
- [112] Robicheaux F and Hanson J 2002 *Phys. Rev. Lett.* **88** 55002
- [113] Gericke D and Murillo M 2003 *Contrib. Plasma Phys.* **43** 298
- [114] Maxson J M, Bazarov I V, Wan W, Padmore H A and Coleman-Smith C E 2013 *New J. Phys.* **15** 103024
- [115] van der Geer S B, Reijnders M P, de Loos M J, Vredendregt E J D, Mutsaers P H A and Luiten O J 2007 *J. Appl. Phys.* **102** 094312
- [116] Pohl T, Pattard T and Rost J M 2004 *J. Phys. B: At. Mol. Opt. Phys.* **37** L183
- [117] Greiner M, Bloch I, Mandel O, Hänsch T W and Esslinger T 2001 *Phys. Rev. Lett.* **87** 160405
- [118] Murillo M S 2001 *Phys. Rev. Lett.* **87** 115003
- [119] Gallagher T F 1994 *Rydberg Atoms* (Cambridge: Cambridge University Press)
- [120] Viteau M, Bason M G, Radogostowicz J, Malossi N, Ciampini D, Morsch O and Arimondo E 2011 *Phys. Rev. Lett.* **107** 060402
- [121] Schauf P, Cheneau M, Endres M, Fukuhara T, Hild S, Omran A, Pohl T, Gross C, Kuhr S and Bloch I 2012 *Nature* **491** 87
- [122] Schwarzkopf A, Sapiro R E and Raithel G 2011 *Phys. Rev. Lett.* **107** 103001
- [123] Schwarzkopf A, Anderson D A, Thaicharoen N and Raithel G 2013 *Phys. Rev. A* **88** 061406
- [124] Bannasch G, Killian T C and Pohl T 2013 *Phys. Rev. Lett.* **110** 253003
- [125] Murphy D, Scholten R E and Sparkes B M 2015 *Phys. Rev. Lett.* **115** 214802

- [126] Pohl T, Pattard T and Rost J M 2005 *Phys. Rev. Lett.* **94** 205003
- [127] McQuillen P, Strickler T, Langin T and Killian T C 2015 *Phys. Plasmas* **22** 033513
- [128] Pohl T, Demler E and Lukin M D 2010 *Phys. Rev. Lett.* **104** 043002
- [129] van Bijnen R M W, Smit S, van Leeuwen K A H, Vredendregt E J D and Kokkelmans S J J M F 2011 *J. Phys. B: At. Mol. Opt. Phys.* **44** 184008
- [130] Schachenmayer J, Lesanovsky I, Micheli A and Daley A J 2011 *New J. Phys.* **13** 059503
- [131] Nogrette F, Labuhn H, Ravets S, Barredo D, Béguin L, Vernier A, Lahaye T and Browaeys A 2014 *Phys. Rev. X* **4** 021034
- [132] Mansbach P and Keck J 1969 *Phys. Rev.* **181** 275
- [133] Comparat D, Vogt T, Zahzam N, Mudrich M and Pillet P 2005 *Mon. Not. R. Astron. Soc.* **361** 1227–42
- [134] Buckanie N M, Göhre J, Zhou P, von der Linde D, Horn-von Hoegen M and Meyer Zu Heringdorf F J 2009 *J. Phys.: Condens. Matter* **21** 314003
- [135] Orloff J 1993 *Rev. Sci. Instrum.* **64** 1105
- [136] Bernal S, Li H, Godlove T, Haber I, Kishek R A, Quinn B, Reiser M, Walter M, Zou Y and O’Shea P G 2004 *Phys. Plasmas* **11** 2907
- [137] Dwyer J R, Hebeisen C T, Ernstorfer R, Harb M, Deyirmenjian V B, Jordan R E and Miller R J D 2006 *Phil. Trans. A* **364** 741
- [138] Siwick B J, Dwyer J R, Jordan R E and Miller R J D 2002 *J. Appl. Phys.* **92** 1643
- [139] Chatelain R P, Morrison V, Godbout C, van der Geer B, de Loos M and Siwick B J 2012 *Ultramicroscopy* **116** 86–94
- [140] Tao Z, Zhang H, Duxbury P M, Berz M and Ruan C Y 2012 *J. Appl. Phys.* **111** 044316
- [141] Kirchner F O, Gliserin A, Krausz F and Baum P 2013 *Nat. Photon.* **8** 52
- [142] Luiten O J, van der Geer S B, de Loos M J, Kiewiet F B and van der Wiel M J 2004 *Phys. Rev. Lett.* **93** 094802
- [143] Reiser M, O’Shea P, Bernal S and Kishek R 2008 *Theory and Design of Charged Particle Beams* (New York: Wiley)
- [144] Kapchinskii I M and Vladimirskii V V 1969 *Proceedings of the International Conference on High Energy Accelerators* (Geneva: Scientific Information Service CERN)
- [145] Van Oudheusden T, De Jong E, van der Geer S, Op’t Root W, Luiten O and Siwick B 2007 *J. Appl. Phys.* **102** 093501
- [146] Van Oudheusden T, Pasmans P, van der Geer S, De Loos M, Van Der Wiel M and Luiten O 2010 *Phys. Rev. Lett.* **105** 264801
- [147] Tokita S, Hashida M, Inoue S, Nishoji T, Otani K and Sakabe S 2010 *Phys. Rev. Lett.* **105** 215004
- [148] Li Y and Lewellen J 2008 *Phys. Rev. Lett.* **100** 074801
- [149] Li Y, Chemerisov S and Lewellen J 2009 *Phys. Rev. Spec. Top.—Accel. Beams* **12** 020702
- [150] Serafini L 1992 *AIP Conf. Proc.* **279** 645
- [151] Serafini L 1997 *AIP Conf. Proc.* **321** 321
- [152] Musumeci P, Moody J, England R, Rosenzweig J and Tran T 2008 *Phys. Rev. Lett.* **100** 244801
- [153] Moody J, Musumeci P, Gutierrez M, Rosenzweig J and Scoby C 2009 *Phys. Rev. Spec. Top.—Accel. Beams* **12** 070704
- [154] Piot P, Sun Y E, Maxwell T J, Ruan J, Secchi E and Thangaraj J C T 2013 *Phys. Rev. Spec. Top.—Accel. Beams* **16** 010102
- [155] van Bijnen R M W, Ravensbergen C, Bakker D J, Dijk G J, Kokkelmans S J J M F and Vredendregt E J D 2015 *New J. Phys.* **17** 023045
- [156] Musumeci P, Moody J T and Scoby C M 2008 *Ultramicroscopy* **108** 1450–3
- [157] Abbey B *et al* 2011 *Nat. Photon.* **5** 420–4
- [158] Flewett S, Quiney H M, Tran C Q and Nugent K A 2009 *Opt. Lett.* **34** 2198–200
- [159] Whitehead L, Williams G, Quiney H, Vine D, Dilanian R, Flewett S, Nugent K, Peele A, Balaur E and McNulty I 2009 *Phys. Rev. Lett.* **103** 243902
- [160] Viteau M *et al* 2016 *Ultramicroscopy* **164** 70–7